Probing the role of the galactic environment in the formation of stellar clusters, using M83 as a test bench

A. Adamo,[1]⋆ J. M. D. Kruijssen,[2] N. Bastian,[3] E. Silva-Villa[4] and J. Ryon[5]

[1]*Department of Astronomy, Oskar Klein Centre, Stockholm University, AlbaNova University Centre, SE-106 91 Stockholm, Sweden*
[2]*Max-Planck-Institut für Astrophysik, Karl-Schwarzschild-Strasse 1, D-85748 Garching, Germany*
[3]*Astrophysics Research Institute, Liverpool John Moores University, 146 Brownlow Hill, Liverpool L3 5RF, UK*
[4]*Instituto de Fsica-FCEN, Universidad de Antioquia, Calle 70 No. 52-21, Medellin, Colombia*
[5]*Department of Astronomy, University of Wisconsin-Madison, 475 N. Charter St., Madison, WI 53706, USA*

ABSTRACT

We present a study of the M83 cluster population, covering the disc of the galaxy between radii of 0.45 and 4.5 kpc. We aim to probe the properties of the cluster population as a function of distance from the galactic centre. We observe a net decline in cluster formation efficiency (Γ, i.e. amount of star formation happening in bound clusters) from about 26 per cent in the inner region to 8 per cent in the outer part of the galaxy. The recovered Γ values within different regions of M83 follow the same Γ versus star formation rate density relation observed for entire galaxies. We also probe the initial cluster mass function (ICMF) as a function of galactocentric distance. We observe a significant steepening of the ICMF in the outer regions (from -1.90 ± 0.11 to -2.70 ± 0.14) and for the whole galactic cluster population (slope of -2.18 ± 0.07) of M83. We show that this change of slope reflects a more fundamental change of the 'truncation mass' at the high-mass end of the distribution. This can be modelled as a Schechter function of slope -2 with an exponential cutoff mass (M_c) that decreases significantly from the inner to the outer regions (from 4.00 to 0.25×10^5 M$_\odot$) while the galactic M_c is $\approx 1.60 \times 10^5$ M$_\odot$. The trends in Γ and ICMF are consistent with the observed radial decrease of the $\Sigma(\text{H}_2)$, hence in gas pressure. As gas pressure declines, cluster formation becomes less efficient. We conclude that the host galaxy environment appears to regulate (1) the fraction of stars locked in clusters and (2) the upper mass limit of the ICMF, consistently described by a near-universal slope -2 truncated at the high-mass end.

Key words: galaxies: spiral – galaxies: star clusters – galaxies: star formation.

1 INTRODUCTION

Young star clusters are potentially bright, long-lived, tracers of star formation within their host galaxies. It is therefore of paramount importance to understand what governs the cluster formation process (e.g. Longmore et al. 2014) and how the host galactic environment may affect their formation and evolution (e.g. Adamo & Bastian 2015).

Statistically, we can describe the cluster formation as a stochastic process. Numerous works report of an initial cluster mass and luminosity function (ICMF and ICLF, respectively) being described with good approximation by a single power-law slope of index close to -2 (e.g. Bik et al. 2003; de Grijs et al. 2003; Whitmore, Chandar & Fall 2007; Chandar et al. 2014; Whitmore et al. 2014). The stochastic nature of cluster formation combined with the power-law distributions of the cluster mass generates the so-called size-of-

sample effects. These effects are well described by the positive relations between the number of clusters (Whitmore 2000) or the youngest brightest cluster in the V band, M_V^{bright}, and the galactic star formation rate (SFR; Larsen 2002; Bastian 2008). In other words, galaxies with higher SFR have more numerous cluster populations; therefore, they are more likely to sample the ICMF at higher mass (luminosity) ranges. The size-of-sample effect also applies to the time-binning of the cluster population. Massive clusters are statistically more likely to be older because the galaxy has had a longer period of time to sample the high-mass bins of the ICMF (Hunter et al. 2003).

Increasing evidence, however, suggests that this is not the full picture. A steepening at the bright luminosity bins of the ICLF has widely been observed and reported (e.g. Whitmore et al. 1999, 2014; Larsen 2002; Gieles et al. 2006b; Bastian et al. 2012). This steepening could be explained by the presence of a truncation at the high-mass end of the ICMF (Gieles et al. 2006b). Indeed, the presence of a truncation mass may explain why we do not observe

⋆ E-mail: adamo@astro.su.se
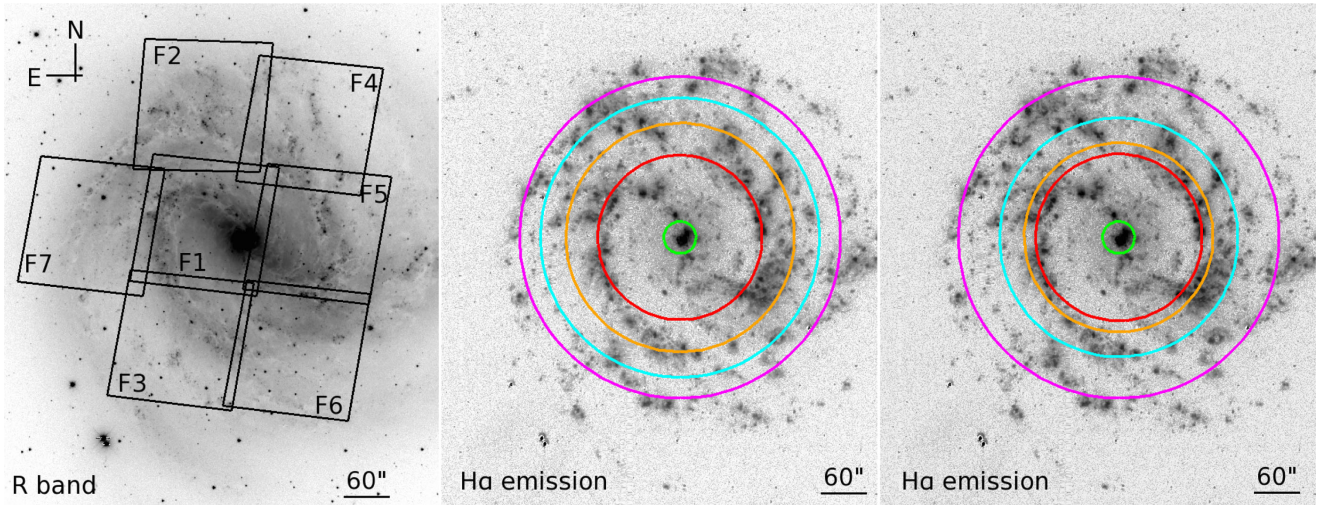
Figure 1. Left: M83 image in the red visual band (*R* band); the footprints of the seven *HST* pointings necessary to cover the bulk of the galactic body are overlaid. Centre and right: the Hα continuum-subtracted image of M83 shows the regions where the current star formation is occurring in the galaxy. Annuli of equal area (centre) and containing equal number of clusters (right) are overplotted. The central region, contained inside the green circle, has been excluded from the analysis. Orientation and resolution of the images are indicated on each frame. Image credit at Dale et al. (2009), taken from NASA/IPAC Extragalactic Database (NED).

very massive young star clusters close to 10^6 M$_\odot$ mass in the Milky Way (Larsen 2006). However, it is difficult to establish the presence of a truncation due to low number statistics (Larsen 2006). Several works report an ICMF compatible with a Schechter function of slope -2 and an exponential cutoff at masses above a certain characteristic mass, M_c (e.g. Larsen 2009; Bastian et al. 2012; Konstantopoulos et al. 2013). Interestingly, it has been observed by these authors that M_c may change as a function of the host galactic environment. Such an environmental dependence would be expected theoretically due to the variation of the maximum mass scale for gravitational instability in galaxy discs (the 'Toomre mass'; Toomre 1964), which should lead to an increase of the maximum cluster mass with the gas pressure (Kruijssen 2014).

More evidence of the role played by the galactic environment in the properties of their cluster population has indirectly been suggested by the so-called T_L(U) versus SFR relation (Larsen 2002; Adamo, Östlin & Zackrisson 2011). T_L(U) is the fraction of *U*-band light locked in star clusters with respect to the total *U*-band light of the galaxy. This fraction is observed to increase as a function of the SFR of the galaxy, suggesting that the fraction of star formation happening in clusters (hereafter Γ or cluster formation efficiency, CFE) is increasing (Adamo & Bastian 2015). Indeed direct evidence of a varying CFE as a function of the average galactic star formation rate density (Σ_{SFR}) has been observed in numerous galaxies (e.g. Goddard, Bastian & Kennicutt 2010; Adamo et al. 2011; Annibali et al. 2011; Ryon et al. 2014, among many others).

In the model proposed by Kruijssen (2012), a variation in the CFE is directly linked to the star and cluster formation process itself. This model describes star and cluster formation continuously across the density spectrum of the hierarchically structured interstellar medium (ISM), in which the highest star formation efficiencies (and thus bound stellar fractions) are reached in the highest density peaks.[1] Integration of these local physics over the gas density

spectrum then results in a CFE that increases with the gas surface density or pressure, as well as the SFR density (Kruijssen 2012). Given the density gradient observed in disc galaxies, the model thus predicts that the CFE decreases with the galactocentric radius. Indeed, using a small fraction of the whole cluster population of M83, Silva-Villa, Adamo & Bastian (2013, hereafter SV13) report evidence of such a variation of the CFE as a function of galactocentric distances.

The aim of this paper is to probe the imprints that the galactic environment leaves on the properties of its cluster population. The results will shed light on how the star cluster population is a natural outcome of the physics driving galactic star formation, and will also help to use star cluster populations as tracers of the star formation history (SFH) of their host galaxies. To achieve this goal, we study the cluster population of the nearby (~4.5 Mpc, corresponding to a distance modulus of 28.28 mag) spiral galaxy M83. This galaxy hosts a rich cluster population which has been widely analysed in recent years (Chandar et al. 2010; Bastian et al. 2011, 2012; Silva-Villa & Larsen 2011; Whitmore et al. 2011; SV13; Silva-Villa et al. 2014; Chandar et al. 2014; Hollyhead et al. 2015). Several studies suggest that the current ongoing starburst at the centre of this galaxy (e.g. Wofford, Leitherer & Chandar 2011) was mostly likely produced by a recent minor merger (Knapen et al. 2010). Outside this region the most active star-forming regions in the galaxy are at the end of the bar (see Fig. 1). However, we notice that star formation is occurring over the entire spiral arm system and in spurs extended inside the inter-arm regions, as in M51 (Chandar et al. 2011).

Only recently M83 has been fully observed with the *Hubble Space Telescope* (*HST*) with broad and narrow imaging bands covering from the UV to the NIR and several optical emission lines (Blair et al. 2014). Previous studies of the cluster population have therefore focused on the two pointings F1 and F2 (see Fig. 1). Chandar et al. (2010, 2014) report of a similar ICMF and cluster disruption rate in both inner (F1) and outer (F2) fields. They notice a steepening of the ICMF slope and a milder disruption rate in F2, but they conclude that within the uncertainties the results support a cluster formation and evolution scenario independent of the galactic environment. With a

---

[1] In addition, tidal heating by encounters with giant molecular clouds (GMCs) imposes a minimum density for the formation of bound clusters, which in practice is only important in the very highest density environments.

similar cluster catalogue comparison presented in both Bastian et al. (2012); Chandar et al. (2014) – Bastian et al. (2011, 2012, hereafter B12) point out the differences in the photometric properties, ICMF and ICLF, and disruption rate of the cluster populations in the two pointings. The differences cannot be accounted for by a recent, significant change in the SFH, so are therefore most likely linked to the cluster formation and disruption properties of the local galactic environment. Such a change in cluster properties is also supported by the change in the CFE as a function of distance from the centre of the galaxy observed by SV13.

The access to a full cluster catalogue for M83 now allows us to verify and put stronger constraints on previous findings. Using the whole M83 cluster catalogue, Silva-Villa et al. (2014, hereafter SV14) find a clear environmental dependence on the strength of the cluster disruption with higher cluster disruption in the inner regions of the galaxy, as already suggested by B12. In a recent publication, Hollyhead et al. (2015) have studied the Hα morphology of the very young star clusters in M83, reporting that clusters are already partially or fully exposed within a few Myr after their formation. Ryon et al. (2015) have focused on the analysis of M83 cluster sizes, important for the dynamical evolution of these systems. In the present work, we will expand the ICMF analysis published by B12 and the analysis of the CFE by SV13 to the whole cluster population within the M83 disc. All together, these works present an unprecedentedly detailed and complete study of the cluster population of a nearby galaxy.

The paper is organized as follows. Section 2 describes the photometric analysis and the properties of the final cluster catalogue. We also include a description of the ancillary data used in the analysis. In Section 3, we present our results. Section 4 contains a discussion of the results within the wider context of cluster and star formation in galaxies. A summary of the paper is presented in Section 5.

2 DESCRIPTION OF THE DATA

2.1 The cluster catalogue

This analysis is based on the complete M83 cluster catalogue recently published in SV14. The final cluster catalogue has been obtained from two multiband *HST* imaging data sets (GO 11360, PI: O'Connell, and GO 12513, PI: Blair). The two combined data sets cover within seven pointings the face-on M83 disc up to a distance of 4.5 kpc (3.4 arcmin) from the centre of the galaxy (see Fig. 1 and Table 1). Our analysis is based on wide field camera 3 (WFC3) imaging in five optical bands, $F336W$ (hereafter U band), $F438W$ (B band), $F555W$ or $F547M$ (V band), $F657N$ (narrow filter centred on Hα) and $F814W$ (hereafter I band). Cluster detection has been performed on the V band with optimized parameter inputs of the source extraction algorithm SEXTRACTOR (Bertin & Arnouts 1996). For each extracted source, aperture photometry has been performed in all the bands with an aperture radius of 5 pixels (0.2 arcsec $\sim$ 4.4 pc) and a sky annulus located at 8 pixels (0.32 arcsec) and 2 pixels (0.08 arcsec) wide. Isolated compact clusters, visually selected, were used to estimate and add the amount of missed flux lost because of the small aperture size used. Moreover, small differences in calibration between different pointings were corrected as explained in SV14. The final catalogue retains only sources with a concentration index larger than 1.25 mag and positive detections in four filters (*UBVI*). We consider detection in Hα as additional but not required constraint. The Vega zero-points used to flux calibrate the photometry

Table 1. Description of the *HST* data set used in this analysis. All the data have been taken with the WFC3. The exposure time of each band is included in parentheses. $N_{\rm cl}$ is the final number of clusters (class 1 and 2) in each field. We include within parentheses how many of these clusters belong to class 1.

Field	PI	Filters	$N_{\rm cl}$ [a]
F1	O'Connell	$F336W$ (1890 s), $F438W$ (1880 s) $F555W$ (1230 s), $F657N$ (1484 s) $F814W$ (1213 s)	1387 (672)
F2	O'Connell	$F336W$ (2560 s), $F438W$ (1800 s) $F547M$ (1203 s), $F657N$ (1484 s) $F814W$ (1213 s)	1098 (547)
F3	Blair	$F336W$ (2579 s), $F438W$ (1799 s) $F547M$ (2682 s), $F657N$ (1799 s) $F814W$ (1379 s)	1142 (595)
F4	Blair	$F336W$ (2589 s), $F438W$ (1809 s) $F547M$ (2682 s), $F657N$ (1809 s) $F814W$ (1389 s)	1243 (687)
F5	Blair	$F336W$ (2589 s), $F438W$ (1809 s) $F547M$ (2682 s), $F657N$ (1809 s) $F814W$ (1389 s)	1199 (676)
F6	Blair	$F336W$ (2579 s), $F438W$ (1799 s) $F547M$ (2682 s), $F657N$ (1799 s) $F814W$ (1379 s)	1414 (774)
F7	Blair	$F336W$ (2579 s), $F438W$ (1799 s) $F547M$ (2682 s), $F657N$ (1799 s) $F814W$ (1379 s)	859 (521)

Notes. [a]The clusters located within 0.45 kpc from the centre have not been included in this final catalogue.

have been retrieved from the WFC3 instrument webpage.[2] Milky Way foreground extinction correction has been applied (Schlafly & Finkbeiner 2011). As described in SV14, the initial catalogue has been visually inspected and each source has been assigned a flag describing the morphology of the cluster. Class 1 objects are clusters with symmetric and compact light distribution. Class 1 objects are most likely bound clusters as tested in B12. Class 2 objects show asymmetries in the light distribution, multiple peaks and potentially contaminant neighbours. These objects closely resemble OB associations; therefore, there is a fair chance of them being unbound (Gieles & Portegies Zwart 2011). Class 3 objects are spurious detections (bad pixels mostly located at the end of the chip, background and foreground sources) and have been removed from the final catalogue. Any cluster candidate located within a radius of 0.45 kpc has also been excluded from the catalogue. We excluded this region because of the high luminosity gradient which causes a change in the completeness of the cluster detection and because of the different SFH that this region has experienced (B12). The number of cluster candidates detected in each field is listed in Table 1.

2.2 Physical cluster properties

The observed spectral energy distribution (SED) of each object, reconstructed from the observed integrated fluxes in all the bands, has been compared to stellar evolutionary models including treatment of nebular gas emission and continuum (*Yggdrasil* models; Zackrisson et al. 2011). The fitting algorithm is described in Adamo et al.

[2] http://www.stsci.edu/hst/wfc3/phot_zp_lbn

(2010). The model fluxes are reddened according to the Cardelli, Clayton & Mathis (1989) prescription. The algorithm simultaneously fits age and extinction of the cluster, while the mass is the normalization factor to scale the models to the observed SEDs. Uncertainties on the derived ages, masses and extinction are estimated according to the recipe presented in Adamo et al. (2012).

Although final cluster catalogues for F1 and F2 were available (B12), we decided to repeat the analysis for these two fields to make the data set as homogeneous as possible. The comparison with the B12 catalogue shows some minor differences in the ages of the clusters between the latter catalogue and the new one as reported in SV14. The difference was produced by an erroneous extinction value systematically applied to the *I* band which was a factor of 1.26 higher than the correct one. The cluster catalogue, published in this work, contains the correct and most updated cluster photometry and properties for M83. As already discussed in SV14 and in the present work, the main conclusions reached in B12 and SV13 are not affected by this error.

2.3 Estimates of the SFRs

In this work, we have estimated current (between 1 and 10 Myr) and average (between 10 and 50 Myr) star formation rates (cSFR and ⟨SFR⟩, respectively) in different regions of the galaxy as follows. The SFR is compared to the cluster formation rate (CFR) to derive Γ. Since clusters have been detected in optical wavelengths, we derive SFRs from optical tracers. Thus, we use Hα as tracer of the cSFR and stellar counts to derive the recent SFH (up to 50 Myr). This choice may not take into account the hidden SFR better captured by an IR tracer; however, our SFR estimates will suffer similar extinction patterns as the clusters do, cancelling out the effects.

To estimate the cSFR in different regions of the galaxy, we used the publicly available Hα continuum-subtracted image of M83 (see Dale et al. 2009, for details on the reduction process and calibration). We calibrated the total luminosity estimated from this frame (after masking residuals at the location of foreground stars) to the total Hα luminosity published by Kennicutt et al. (2008), giving us a correction factor that takes into account [N II] contamination and foreground galactic extinction. An average visual extinction of $A_V \sim 0.2$ mag has been applied to the total Hα flux. To convert Hα luminosity into SFR, we use the relation by Kennicutt & Evans (2012).

To estimate the ⟨SFR⟩, we derive the recent SFH using colour–magnitude diagrams of the resolved stellar population. The technique and method are described in Silva-Villa & Larsen (2012) and SV13. Stellar photometry and analysis will be discussed in a forthcoming paper (Silva-Villa et al., in preparation). For consistency with the cluster and Hα analyses, we corrected the final stellar photometry by an average visual extinction of 0.2 mag. Because of different detection limits between the arm and inter-arm regions, we applied a conservative approach. Completeness tests show that our SFH is robust between 10 and 50 Myr, above and below which the significance of our results drops. The ⟨SFR⟩ is thus derived averaging the SFH over 10–50 Myr.

2.4 Estimates of the gas surface density

To estimate the gas surface density, $\Sigma(H_2)$, we use the velocity-integrated CO(1–0) intensity map published by Lundgren et al. (2004a), to which we refer for a description of the data set and reduction steps. CO intensity was derived within each bin used in our analysis. To convert the CO intensity to a molecular gas mass,

we adopt a conversion factor of $X_{CO} = 2.3 \times 10^{20}$ K km s^{-1} cm^2.[3] The derived values are in good agreement with averaged $\Sigma(H_2)$ reported in their work (Lundgren et al. 2004a).

3 RESULTS

3.1 Analysis approach

To understand how the galactic environment influences star and cluster formation, we analyse and compare the cluster properties in different regions of M83. The galactic region contained between the inner radius of 0.45 kpc and outer radius of 4.5 kpc has been divided into four bins. As shown in the central and right panels of Fig. 1, we choose two binning approaches, equal surface area bins and bins containing the same number of objects (the latter approach already applied in SV13). For each bin, we derive the following quantities (see Table 2): cSFR (1–10 Myr); ⟨SFR⟩ (10–50 Myr); Γ (1–10 Myr) and Γ (10–50 Myr); predicted CFE (Γth); gas surface density, $\Sigma(H_2)$; luminosity of the youngest most massive cluster, M_V^{bright}; mass of the most massive cluster (in the age range 3–100 Myr), M_{max}; characteristic mass, M_c; and slope of the mass function if a single power law is used, α. In Fig. 2, we show the age–mass diagram of the cluster population contained in each bin of equal area. We include both class 1 (red dots) and 2 (black dots) objects. We do not see any significant difference within the two classes and each bin has similar fractions of class 1 versus class 2 objects. The blue and green boxes show the cluster population used to derive the CFE as described below. The age distributions of Fig. 2 clearly show the size-of-sample effect, i.e. the increasing M_{max} as a function of age (and also of decreasing M_{max} as a function of galactocenric distance).

The CFE is defined as the ratio between the CFR and the SFR within the same age interval. We derive the CFR in the same interval used for the SFR (1–10 and 10–50 Myr). The CFR is the ratio between the total stellar mass in clusters and the corresponding age range. The current CFR is estimated from clusters of age between 1 and 10 Myr and cluster mass above a thousand M$_\odot$. This quantity is compared to the cSFR estimated within the same bin to derive Γ (1–10 Myr). Similarly, the average CFR is estimated for clusters with age between 10 and 50 Myr and mass above 5000 M$_\odot$ and directly compared to the ⟨SFR⟩ thus deriving Γ (10–50 Myr).

To derive the total CFR we assume an underlying ICMF power-law of slope -2, with lower and upper mass limits of 100 M$_\odot$ and two times the maximum observed cluster mass in the region under investigation, respectively. The total CFR will be the result of the observed stellar mass in clusters more massive than the observational imposed limit and the missing fraction.

The two mass limits applied at different age ranges to estimate the CFR are well within the detection limits of our sample. They are chosen to be substantially higher than the detection limit to avoid completeness issues. However, these mass limits may cause possible misclassifications due to stochastic effects in the stellar initial mass function (IMF) as pointed out by several studies (e.g. Fouesneau & Lançon 2010; Popescu & Hanson 2010). In an upcoming work, our deterministic approach to derive cluster properties is compared to the predictions obtained by SLUG (Krumholz et al., in preparation).

---

[3] We adopt this value for consistency with Lundgren et al. (2004a). This choice is consistent with the Galactic conversion factor of $X_{CO} = 2.0 \times 10^{20}$ K km s^{-1} cm^2 with an uncertainty of about 30 per cent (Bolatto, Wolfire & Leroy 2013).

Table 2. Galactic and cluster population properties derived for the whole population, in annuli of equal area or containing equal number of clusters. Only class 1 clusters have been used in this analysis. The typical uncertainty on Γ^{theory} is a factor of 2 (see Section 3.2). The M_V^{bright}, M_{max}, M_{c} and α have been derived for class 1 clusters younger than 100 Myr and more massive than 5000 $M_{\odot}$.

Annulus (kpc)	cSFR ($M_{\odot}$ yr^{-1})	$\langle$SFR$\rangle$ ($M_{\odot}$ yr^{-1})	Γ(1–10 Myr) (per cent)	Γ(10–50 Myr) (per cent)	Γ^{th} (per cent)	$\Sigma(\mathrm{H}_2)$ ($M_{\odot}$ pc^{-2})	M_V^{bright} (mag)	M_{max} (10^5 $M_{\odot}$)	M_{c} (10^5 $M_{\odot}$)	α
				Galactic						
0.45–4.50[a]	0.82 ± 0.08	1.20 ± 0.12	18.2 ± 3.0	15.0 ± 1.9	19.0[b]	47.7	-11.60	$1.95^{+0.45}_{-0.29}$	1.60 ± 0.30	−2.18 ± 0.07
				Equal area						
0.45–2.30	0.25 ± 0.02	0.21 ± 0.02	19.3 ± 4.0	26.5 ± 4.0	28.6	62.4	−11.60	$1.48^{+0.22}_{-0.19}$	4.00 ± 0.80	−1.90 ± 0.11
2.30–3.20	0.31 ± 0.03	0.43 ± 0.04	26.0 ± 3.5	19.2 ± 2.6	20.4	34.9	−11.47	$1.95^{+0.45}_{-0.29}$	1.00 ± 0.20	−2.20 ± 0.11
3.20–3.90	0.15 ± 0.02	0.34 ± 0.03	13.1 ± 2.5	9.8 ± 1.6	13.5	19.4	−10.68	$0.59^{+0.19}_{-0.14}$	0.55 ± 0.11	−2.20 ± 0.12
3.90–4.50	0.11 ± 0.01	0.22 ± 0.02	13.7 ± 3.1	8.0 ± 1.5	12.6	17.7	−10.55	$0.29^{+0.04}_{-0.02}$	0.25 ± 0.05	−2.70 ± 0.14
				Equal number						
0.45–2.30	0.26 ± 0.03	0.25 ± 0.02	18.9 ± 4.4	23.2 ± 4.2	28.6	62.4	−11.60	$1.48^{+0.22}_{-0.19}$	50.00 ± 10.00	−1.90 ± 0.11
2.30–2.60	0.12 ± 0.01	0.25 ± 0.02	34.0 ± 5.1	20.8 ± 4.0	26.3	52.6	−11.47	$1.95^{+0.45}_{-0.29}$	1.50 ± 0.30	−2.05 ± 0.12
2.60-3.30	0.21 ± 0.02	0.37 ± 0.04	19.8 ± 3.6	10.8 ± 2.1	17.4	27.6	−10.27	$0.59^{+0.19}_{-0.14}$	0.60 ± 0.12	−2.35 ± 0.13
3.30–4.50	0.23 ± 0.02	0.33 ± 0.03	14.0 ± 2.6	12.6 ± 2.2	13.0	18.3	−10.55	$0.39^{+0.04}_{-0.05}$	0.30 ± 0.06	−2.50 ± 0.13

[a]Properties of the galaxy and cluster population integrated within 0.45 and 4.5 kpc.
[b]Value from Kruijssen (2012).
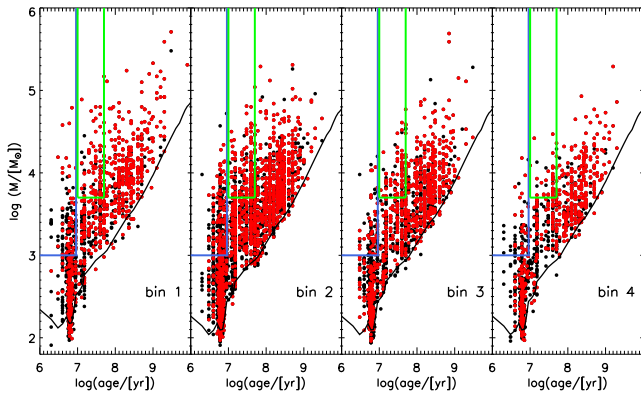
Figure 2. Cluster age versus mass diagram of each bin of equal area. The black dashed lines show the detection limits in the V band ($M_V \leq -5.5$ mag in bin 1 and $M_V \leq -5.3$ mag in the other three bins) and the filter used to extract the source catalogue (see the main text). Black dots are cluster candidates of class 2 and red dots clusters belonging to class 1. The blue and green delimited areas show the clusters used to derive the current and averaged CFR. The limit on the cluster mass is well above the detection limits and has been imposed to mitigate the effect of stochasticity of the IMF.

SLUG is a Bayesian fitting code that uses stochastic IMF models to derive cluster properties (Krumholz et al. 2015). Krumholz et al. (in preparation) find significant misclassification of the cluster mass below 1000 $M_{\odot}$, i.e. the deterministic approach used in this work significantly underestimates cluster masses below a 1000 $M_{\odot}$.

We estimate the fraction of missing stellar mass in clusters with mass below the two thresholds, assuming a power-law slope distribution of -2 and a lower mass limit of 100 $M_{\odot}$ (Longmore et al. 2014). Only class 1 clusters are used to derive CFRs. Due to this conservative approach and the possible effects of stochasticity, our CFE determinations can be considered lower limits to the real values. Monte Carlo simulations of cluster populations are used to estimate the uncertainties associated with the CFR (and hence Γ) values. We take into account a 0.1 dex error in both derived age

and mass of each cluster (uncertainties from the SED fitting technique). We also include the Poissonian likelihood of recovering the observed CFR. This uncertainty accounts for the observed number of clusters within the considered mass and age range as randomly drawn from a power-law cluster mass function with upper mass limit equal to two times the observed maximum mass value in each bin.

In Table 2, one can see that the SFR and Γ derived with different methods agree within 3σ in each bin, confirming that the SFR, as well as the CFE, has not changed significantly in the last 50 Myr (SV14). A different binning of the data does not produce any major impact on the derived quantities. As already discussed in SV13, bins containing the same number of clusters should mitigate the size-of-sample effect. In the M83 case, differences between equal surface area and equal number of cluster bins are mostly restricted to the regions containing a very active site of star formation for the M83 disc, i.e. the edges of the bar (see the central and right panels of Fig. 1). Therefore, even if local variations between the two binning approaches are observed in the central bins covering the end of the bar region, the radial trends discussed in the next sections are preserved.

3.2 On the fraction of star formation happening in clusters as a function of distance within the galaxy

In Fig. 3, we show how Γ changes with galactocentric distances for bins of equal area. The decreasing trend observed here confirms the finding reported by SV13, but for a substantially larger cluster sample. The two Γ values (for each age range) follow each other quite closely. Γ decreases inside out from about 26 to 8 per cent. On different scales (right y-axis), we overplot the gas surface density, $\Sigma(\mathrm{H}_2)$, estimated within the same regions. $\Sigma(\mathrm{H}_2)$ shows a similar decline (black dashed line) suggesting a link between the CFE and the amount of molecular gas available for star formation. The plot also includes the predictions for Γ obtained with the fiducial model by Kruijssen (2012). The model predicts a higher absolute value than the observed one in the centre but agrees quite well with the values we find in the disc, within the uncertainties. We notice that the
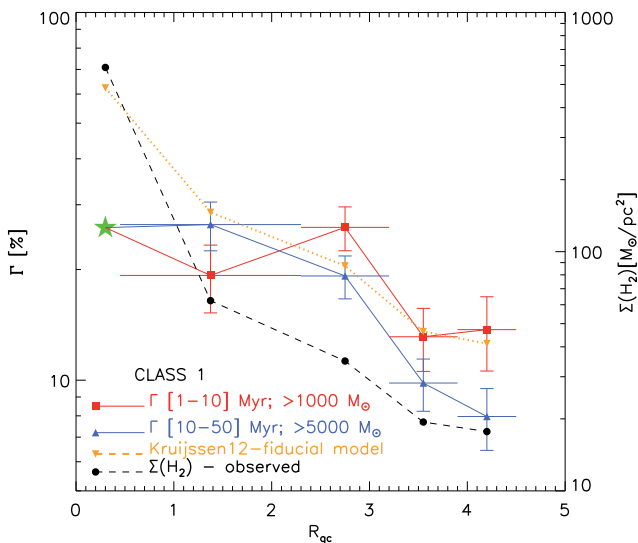
Figure 3. CFE as a function of galactocentric distance. Γ has been estimated for two age ranges and different mass limits as indicated in the inset. Only clusters classified as class 1 have been used for the analysis. Therefore, the CFEs can be considered lower limits to the real fractions. Hα emission is the tracer used to estimate the SFR between 1 and 10 Myr, while direct stellar counts have been used to derive the SFR in the age range 10–50 Myr. The horizontal bars show the width of each annulus. The area within each annulus is the same. The green star shows the Γ value for the starburst region confined in the centre of the galaxy and reported by Goddard et al. (2010). The right-hand y-axis shows the molecular gas surface density (Σ(H₂)). See the text for more details.

inner point (green star symbol), taken from Goddard et al. (2010), is likely to be underestimate due to incompleteness caused by the strong differential extinction in this region. In the disc (between 0.45 and 4.5 kpc), the observed relative decline of Γ is closely reproduced by the model.

The good agreement between the predicted and observed gradients of Γ as a function of galactocentric distance suggests that the Kruijssen cluster formation model can be used to understand the cluster formation process. The model predicts that the formation of bound stellar clusters takes place in the highest density peaks of a hierarchically structured ISM. At these high densities, the gas goes through a large number of free-fall times on a short time-scale and therefore reaches a high star formation efficiency. As a result, the expulsion of any residual gas by feedback does not unbind the stellar distribution (Kruijssen et al. 2012) and a bound cluster survives. At lower densities, the low star formation efficiencies yield unbound associations.[4] Putting these local considerations in a galactic context, the model predicts that clusters form most efficiently at high gas pressures (and hence gas surface densities), because these conditions lead to higher density peaks and thus favour bound cluster formation. In summary, the model thus predicts that the CFE is set by galactic-scale properties such as the gas surface density and, therefore, the star formation rate density Σ_{SFR} through the Schmidt–Kennicutt relation (Kennicutt & Evans 2012).

The two panels in Fig. 4 support the above interpretation. We show the CFE as a function of Σ_{SFR} for our spatially resolved data

---

[4] An additional included effect at high gas surface densities ($\Sigma > 10^3$ M$_\odot$ pc^{-2}) is that tidal perturbations by dense GMCs unbind lower density clusters that otherwise would have survived (cf. Kruijssen et al. 2011).

points in M83 as well as for a compilation of literature measurements of the CFE in entire galaxies. Both the entire galaxies and the different regions within galaxies follow the same trend of increasing CFE with the SFR density. We include the CFEs estimated for the two types of M83 binning (equal area and equal cluster number bins). We also estimate the CFE in each of the seven fields shown in Fig. 1. We show the M83 CFEs for both age ranges (left- and right-hand panels). Overall, the agreement with Kruijssen's fiducial model (black dotted line) is very encouraging and adds to the evidence supporting a tight link between galactic environment and stellar cluster formation.

3.3 Cluster mass function as a function of distance within the galaxy

B12 report evidence of a steepening of the ICMF in the cluster population of F2 relative to that of F1 (see the position of the two fields in the galaxy in Fig. 1). The two cluster populations are better fitted by a Schechter mass function of slope −2 and M_c ∼1.5 × 10⁵ and 0.5 × 10⁵ M$_\odot$ in the inner and outer fields, respectively. Access to a complete cluster catalogue for this galaxy enables us to further investigate how the galactic environment possibly influences the shape of the ICMF. Using the same analysis technique as in the previous section, we construct cumulative distributions of the cluster mass of each radial bin. Cumulative distributions are favoured to avoid any subjectivity in the choice of the mass bin size and because they are more sensitive to variations. Statistically, this method has the same significance of distributions of bins containing the same number of objects (Maíz Apellániz & Úbeda 2005), with our distributions containing only one object per bin. In the previous paragraph, to estimate Γ we have limited our analysis to cluster ages overlapping the age range to which our chosen SFR tracers are sensitive. However, to build the ICMF, we do not need to apply the same limits. Similarly to the limits used by B12 and in other recent works, we apply a lower mass limit of 5000 M$_\odot$ and an age cut between 3 and 100 Myr. For comparison, we generate Monte Carlo simulations of cluster populations with the same cluster numbers of the observations. We assume the same lower mass cutoff as in the observations (5000 M$_\odot$) and an upper limit to the cluster mass of 10⁷ M$_\odot$, which is much larger than the observed maximum cluster mass so it approximates the condition of no upper mass truncation of the ICMF.

We discuss below the results obtained using only class 1 clusters. In Fig. A1 of Appendix A, we include the same analysis but building the ICMFs of both class 1 and 2 objects, instead. The recovered absolute values vary within a factor of 2. Therefore, the observed trends and conclusions remain unchanged confirming that our results are not driven by the selection criteria.

In Fig. 5, we show the observed and simulated ICMFs for the entire cluster population (top row) and for the clusters contained in bins of equal area (second top row to bottom). The results do not change if cluster populations in bins of equal numbers are used instead (see Table 2). Each panel shows the observed cumulative distribution (red dots), the median (black solid line) and the limits containing 50 (dashed lines) and 90 per cent (dotted lines) of the 2000 cumulative ICMF realisations. We use different functions, i.e. single power law of slope −2 and no upper mass limit; single power law of some best-fitting slope that is not necessarily −2; a Schechter function of power-law slope −2 and exponential truncation above a variable characteristic mass, M_c.

To verify the goodness of the agreement between the observed and simulated distributions, we use the Kolmogorov–Smirnov (KS)
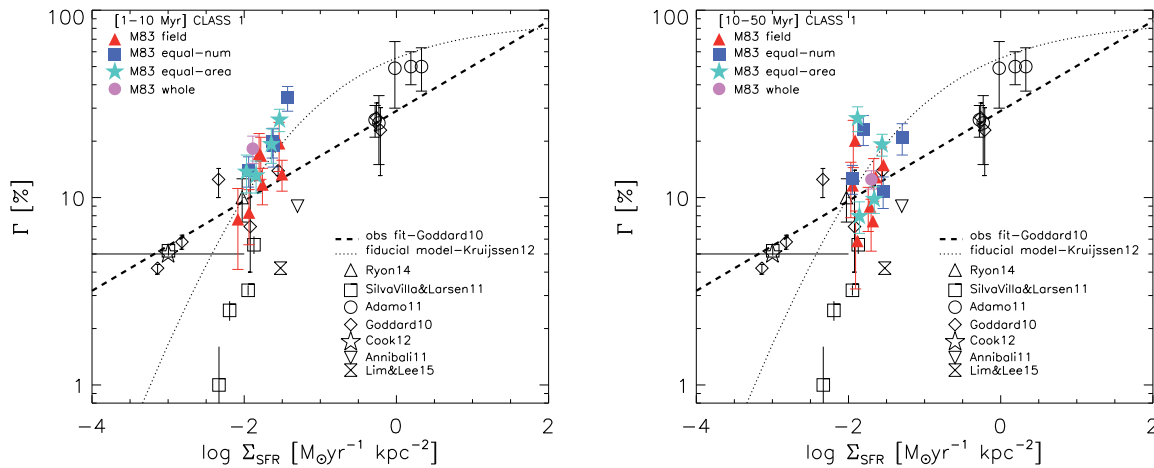
Figure 4. Γ versus SFR surface density for class 1 clusters. The same diagram shows the position of the CFE estimated within different regions of the galaxy (see top inset) using circular bins of same area, annuli containing the same number of clusters and the position of each *HST* pointing (seven fields). On the left plot, Γ has been derived from clusters younger than 10 Myr; on the right plot, from clusters in the age range 10–50 Myr. Literature data and predictions have been included for comparison (see Table B1 in Appendix for references and a complete list of the values used in this plot).

statistic. The resulting probability, $p(\text{KS})$, that the two distributions are actually produced by the same parent population is included in each panel. In the first column, we attempt to reproduce these distributions with a single power-law function of slope -2. The innermost bin cluster mass distribution (top-left panel) is consistent with a power-law function of slope -2. The significance of the deviations from this function increases in the outer bins and the whole M83 cluster population (panels in the first column). The middle-column panels show an attempt to reproduce the ICMFs with single power laws of steeper slopes. We derive the value of the slope which maximizes $p(\text{KS})$. Although the upper mass distributions are not well reproduced by a single power-law function, the KS test favours steeper slopes than the initial value -2.

The change in the slope from ~ -1.9 to -2.7 from the inner to the outermost bin is quite striking. In Table 2, we report the uncertainties associated with the slope in each radial bin as well as for the whole galaxy. We derive the uncertainties on the slopes determining the index interval which contains 68 per cent of the Monte Carlo simulations for each cluster sample. As widely discussed in previous works (e.g. Gieles et al. 2006b), a steepening in the upper mass (luminosity) end of a distribution is often compatible with the presence of a truncation. In the third column, we use a Schechter (1976) function, i.e. $\mathrm{d}N/\mathrm{d}M \propto M^{\alpha} \exp(-M/M_{\mathrm{c}})$, with slope $\alpha = -2$ and variable truncation mass M_{c}, as indicated in the inset of each plot (also see the listed values in Table 2). When using a Schechter function rather than a single power-law slope -2, the agreement between simulations and observations improves for bin 2, bin 3, bin 4 and for the cluster population altogether. This shows that in 80 per cent of the cases, a Schechter function gives a substantially better match to the observed ICMF than a single power-law fit. A unique feature of the Schechter function is the ability to reproduce the observed distributions at the high-mass ends. Statistically a steeper power-law function and a Schechter type function give similar solutions, although the latter seems to be preferred everywhere but the innermost bin. Only there, the KS statistic favours a single power-law fit with a slope slightly less steep than -2, even though this slope cannot be ruled out within the uncertainties. For this reason, the Schechter fit produced with a power-law slope of index -2 does not improve the KS probability. If instead of using a Schechter function with slope -2 we use -1.9, the KS probability

becomes $p(\text{KS}) = 0.58$, which is still lower than the $p(\text{KS}) = 0.794$ obtained for the single power-law fit. In Section 3.4, we discuss the physics driving this difference.

Our results suggest that the ICMF changes significantly as a function of distance from the centre and that the ICMF can be overall described by a power-law function of slope -2 and a decreasing M_{c} as a function of distance from the centre of the galaxy. This finding is in agreement with the analysis presented by B12 for a smaller cluster sample in M83. It clearly suggests that the change in the star formation properties of the galaxy as a function of radius is affecting the shape of the upper mass end of the ICMF.

3.4 The most massive cluster as a function of distance within the galaxy

Widely used in the cluster literature, the brightest cluster luminosity versus the SFR of the galaxy is a relation dominated by the size-of-sample effect (Larsen 2002; Bastian 2008). This relation, as well as the one presented by Whitmore (2000), shows that cluster formation is a stochastic process, i.e. the mass or luminosity of the most massive cluster in a galaxy increases with the SFR, because a larger number of formed clusters in the population increase the probability of forming more massive or luminous clusters. In Fig. 6, we show the SFR versus M_V^{bright} relation including all the data available in the literature. We also add the brightest young cluster recovered in each of the four bins of M83 (purple dots). The dashed black line is a fit to the sample by Larsen (2002) and presented in Weidner, Kroupa & Larsen (2004). Using Monte Carlo simulations under the assumption that only a relative small fraction of star formation is happening in clusters ($\Gamma \sim 8$ per cent), Bastian (2008) reproduces the observed trend. If all star formation would happen in clusters, then the observed points should follow the dotted line on the left side of the dashed one. The scatter of the data points is quite large. Many factors can affect the location of cluster samples in this diagram, such as a recent change in the SFH of the galaxy (Bastian 2008) or a difference in the Γ of each galaxy (Adamo et al. 2011).

Even though the SFR versus M_V^{bright} relation is mainly driven by the size-of-sample effect, i.e. the stochastic sampling of the most massive and luminous clusters from the ICMF, this does not rule out that the galactic environment still plays an important role in shaping
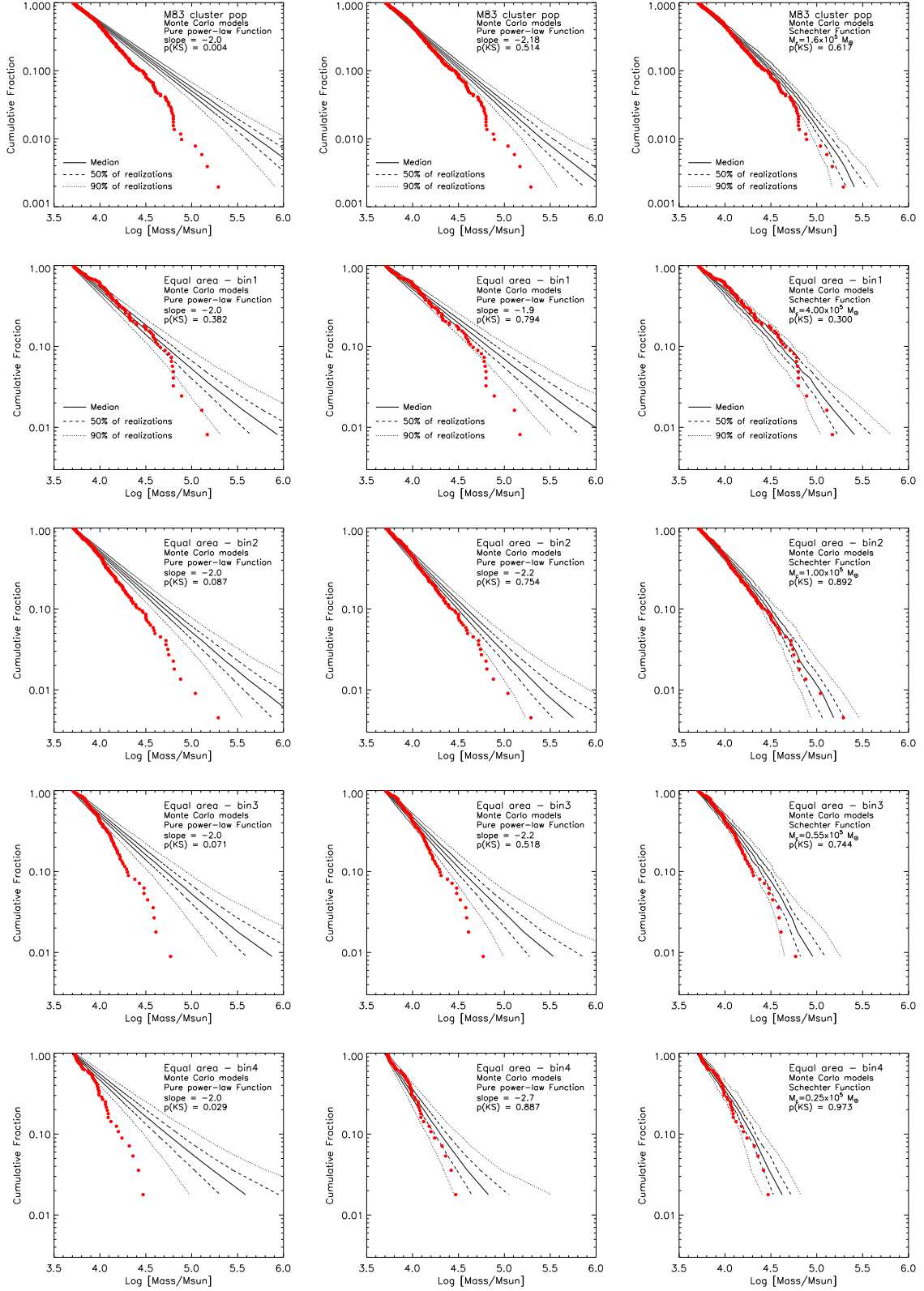
Figure 5. Cumulative ICMFs (red filled dots) of the whole population and of the clusters within bins of same area (from top to bottom). Only clusters classified as 1 (see Fig. A1 in Appendix for the same plots but class 1 and 2 instead), more massive than 5000 $M_\odot$ and ages between 3 and 100 Myr have been included. Median (solid line), quartiles (dashed line) and extended boundaries (dotted line) of Monte Carlo simulations of cluster populations with the same number of objects as the observed ones are included in each panel. In the first column, we assume a pure power-law ICMF with slope -2. In the middle column, we still assume a power-law ICMF but with varying slopes (see insets), chosen to maximize the KS probability that the observed and simulated distributions are drawn from the same parent distribution, p(KS). In the right column, we assume that the ICMF is better described by a Schechter function of slope -2 and an exponential cutoff, M_c, chosen to maximize p(KS).
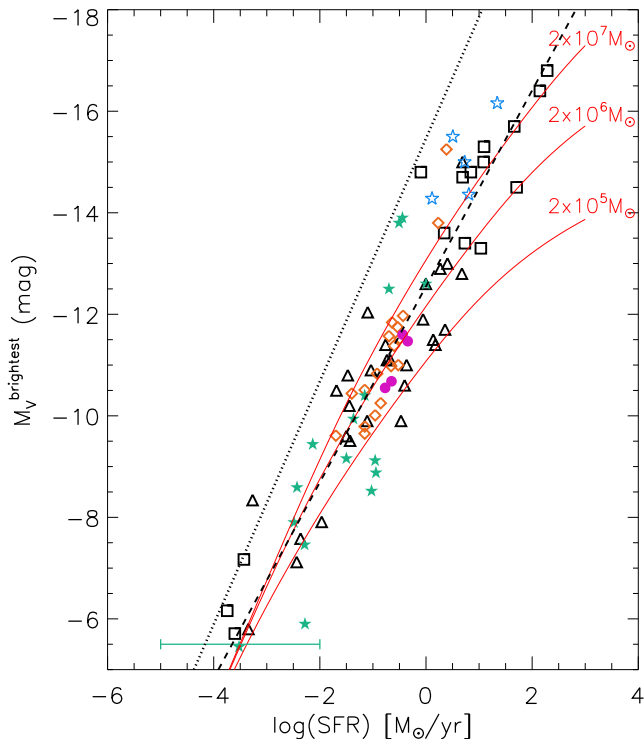
Figure 6. The luminosity of the brightest cluster plotted against the SFR of the host galaxy. This plot contains a compilation of all data available in the literature. See Table B1 in Appendix B for a detailed description of the data sets. The dashed line is the best fit to the sample of galaxies plotted as triangles (Larsen 2002). The dwarf galaxy sample is represented by green filled stars (see Adamo & Bastian 2015, for a description of the sample). Squares are the sample added by Bastian (2008), who derived the expected SFR versus M_V^{bright} relation if 100 per cent of stars are born in clusters with a power-law ICMF with index −2 (black dotted line). Blue stars are the sample of luminous blue compact galaxies studied by Adamo et al. (2011). The green horizontal bar shows the range of SFR of dwarfs which do not have young clusters (Cook et al. 2012). The M83 brightest young clusters of each of the four bins of equal area are plotted as purple circles. The orange diamonds show the sample from Whitmore et al. (2014). The red solid lines show Monte Carlo simulations of cluster populations formed with a Schechter ICMF with different M_c and a CFE of 8 per cent.

the properties of the cluster population (see Section 4). In Fig. 6, we include new Monte Carlo simulations of cluster populations formed with a Schechter ICMF of different M_c assuming a fixed CFE of 8 per cent (red solid lines). The presence of a truncation mass in the ICMF clearly introduces a bend in the simulated SFR versus M_V^{bright} relation. However, this bend is absent in the observed SFR versus M_V^{bright} relation, because galaxies with higher SFRs tend to have higher truncation masses M_c (see below).

The presence of a varying upper mass cutoff in the ICMF is supported by observations of GMCs in local galaxies. In the M51 galaxy, Colombo et al. (2014) report clear differences in the number, mass, luminosity, density and mass distributions of GMCs within different environments of the galaxy (e.g. inter-arm and arm regions, molecular ring, etc.). The mass of the most massive GMC in M51 changes as a function of the galactic environment. With a similar argument, Larsen (2009) noticed that the maximum GMC mass observed in the Antennae system is larger than the GMC mass found in local spiral galaxies. Clusters form within GMCs, and their final mass is a fraction of the total mass of the GMC. The total fraction
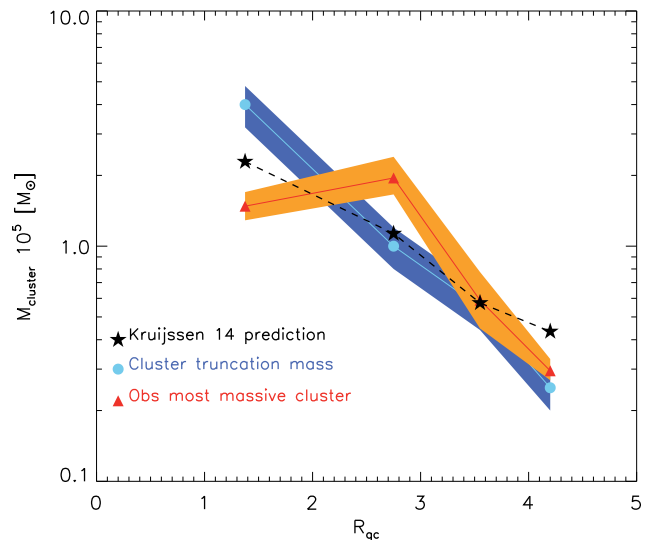
Figure 7. The mass of the most massive cluster found in each bin of same area is plotted as a function of galactocentric distance (red triangles). The shadowed area in orange shows the uncertainties on the mass estimates. The M_c derived in Fig. 5 are plotted using cyan dots, while the blue band shows 20 per cent tolerance margin for the derived values. The predicted cluster M_T are included as black stars (see the text and Kruijssen 2014).

of gas mass converted into stars is usually described by the star formation efficiency, which observations of galactic star-forming regions suggest is only of a few per cent (e.g. Elmegreen 2002; Evans et al. 2009). The maximum fraction of the GMC mass that can end up in a single, most massive cluster then requires this star formation efficiency to be multiplied by the CFE (Kruijssen 2014). The observation of an ICMF truncation mass at the high-mass end is possibly linked to the limit imposed by the galactic environment to the maximum mass that GMCs can have. Theory predicts that this mass scale should correspond to the maximum mass able to overcome the galactic differential rotation and undergo collapse [i.e. the Toomre (1964) mass, see Kruijssen 2014 and references therein].

In Fig. 7, we show the observed maximum cluster mass within each bin in M83 (red triangles and mass uncertainties derived from SED fitting), the recovered M_c including 20 per cent uncertainties and predicted maximum cluster mass scale using equation 3 from Kruijssen (2014, black symbols). It is important to stress here that although we refer to M_c as a truncation, it is not a sharp limit. The truncation of a Schechter function reflects an exponential decay of the probability distribution at the high-mass end. The chances of having clusters more massive than M_c are lower than the case when a pure power-law function of slope −2 is used (Larsen 2009). Indeed, we see that the observed M_{max} and the recovered M_c are in agreement within a factor of 2. To derive the predicted maximum cluster mass we use the averaged Γ (mean of the values at 1–10 and 10–50 Myr) observed in each bin of equal area and we assume that the GMC mass changes between 2 and 0.8×10^7 M$_\odot$[5] (Lundgren

---

[5] We prefer using the observed maximum cloud masses rather than calculating the Toomre mass using the velocity dispersion profiles from Lundgren et al. (2004b). These authors discuss that beam smearing yields velocity dispersions which (especially at small galactocentric radii of <2 kpc) can be overestimated by a factor of 2. This would subsequently lead to severely overestimated Toomre masses ($M_T \propto \sigma^4$) by up to an order of magnitude.

et al. 2004b) in each bin and fix the star formation efficiency to 5 per cent. In spite of the approximations, the predicted and the observed trend agree remarkably well, supporting the role of the galactic environment in shaping the upper mass limits of the ICMF.

4 DISCUSSION

In this work, we probe the impact of the environment on the cluster formation process. Our analysis reinforces previous findings and presents unambiguous imprints left by the M83 galactic environment on its own cluster population.

Cluster formation is a stochastic process; however, the efficiency of the process, i.e. the amount of star formation locked in bound star clusters, varies as a function of the Σ_{SFR}. Several works have shown this link on galactic scales (e.g. Goddard et al. 2010; Adamo et al. 2011, among many others). This effect is also observed on sub-galactic scales, when looking at different regions of the same galaxy (e.g. SV13; Ryon et al. 2014), and our new analysis confirms this result. We find that the cluster formation process is tightly linked to the gas surface density, just like the SFR density is via the Schmidt–Kennicutt relation (Schmidt 1959; Kennicutt 1998). As the gas pressure increases (and hence the gas or SFR surface density), the density spectrum of the ISM broadens and a larger fraction of the density fluctuations reaches densities high enough to collapse on short time-scales and achieve high star formation efficiencies. This locally more efficient star formation enables the young stellar structure to remain bound when any residual gas is expelled (Kruijssen 2012). As a result, the CFE increases with the gas pressure, gas surface density and through the Schmidt–Kennicutt relation also with the SFR density.

However, Γ appears to not grow indefinitely as it obviously cannot attain values exceeding 100 per cent. At gas densities above $\Sigma(H_2) > 1000\,M_\odot\,pc^{-2}$ (which corresponds to $\Gamma \sim 70$ per cent), Γ will not increase significantly (see the dotted line in Fig. 4; Kruijssen 2012). Denser gas favours star and cluster formation but at the same time destroys low-density systems more easily via GMC encounters. These tidal perturbations imply that a CFE of 100 per cent is never reached.

The presence or absence of a truncation at the high-mass end of the ICMF has been long debated in the literature. With simple numerical simulations, Larsen (2006) shows why it is so challenging to prove the presence of a truncation. For example, in Section 3.3, we find that the ICMF of the innermost bin can be well described by a single power-law mass function of slope -1.90 ± 0.11. However, the presence of a truncation cannot be ruled out from the KS test. Large cluster populations are necessary to well sample the high-mass end of the ICMF, but in local galaxies cluster populations have usually a few hundred objects (Larsen 2006). Some previous works in the past have found evidence of a possible truncation and/or variation of the ICMF within the same galaxy (e.g. Larsen 2009; B12; Konstantopoulos et al. 2013) or steepening of the cluster luminosity function (recently Whitmore et al. 2014). In our work, we observe a clear steepening of the ICMF, well represented by a Schechter-type distribution of slope -2 and a variable M_c as a function of distance from the centre of the galaxy. The Schechter function combines the power-law slope and the presence of a limit above which the probability to form more massive clusters goes exponentially to zero. It is not a sharp limit. Interestingly, we observe a clear decline of M_c within the same galaxy. As for the CFE, the decrease of the truncation mass is most likely related to the gradient of the gas pressure (and hence gas and SFR surface density). The

galactic environment thus poses a direct limit on the maximum possible mass scales of GMCs and stellar clusters.

The globular cluster mass function has been reported to be well fitted by an evolved Schechter function by Jordán et al. (2007). This function takes into account the stellar mass loss suffered by globular clusters at the low-mass end of the mass function as well as the steep, non-Gaussian decline at the high-mass end. The M_c of each globular cluster population increases with the total B-band luminosity (mass) of the host galaxy. Dynamical friction alone is not able to reproduce the observed decline of M_c for lower luminosity galaxies suggesting that a link between M_c and the host galaxy at the moment the globular cluster mass function was created.

The results reported in our analysis of M83 and supported by evidence found in previous works can shed light on the cluster formation process not only in local galaxies but also at high redshift. The young star cluster mass function can be described by an almost universal ICMF of slope -2 and a variable M_c which appears to be a function of the host galaxy environment, in that it increases with the gas pressure. Combining this with the aforementioned increase of the truncation mass of the globular cluster mass function with the host galaxy mass, we infer that the gas pressure at the time of globular cluster formation likely increased with the host galaxy mass, as is indeed proposed by recent models (Kruijssen 2015). Our results can help to understand the physical process under which globular clusters formed. Both young and ancient cluster populations can potentially be used as tracers of the star formation process of their host galaxies. However, it is important to keep in mind that the physical conditions of the ISM where globular clusters have formed are quite different and nowadays observed only in merging starburst systems (e.g. Holtzman et al. 1992; Whitmore et al. 1993). Moreover, globular cluster populations have most likely survived because during merging events they have been relocated in the haloes of their galaxies, thereby escaping the gas-rich, disruptive bodies of their host galaxies (Kruijssen 2015). For instance, the M83 cluster population will be affected by cluster disruption according to the results of SV14. In the absence of major events which could move clusters out of the disc, this population will not survive for a Hubble time.

5 CONCLUSIONS

The aim of this work is to probe the link between cluster formation, the observed statistical cluster properties and the galactic environment where they form and interact. With respect to previous analyses, we now have access to a complete cluster catalogue covering the vast majority of the M83 galaxy. We have estimated the CFE across the whole disc of M83 using several techniques and SFR tracers. We have sliced the cluster catalogue into four bins either containing the same number of clusters (as done by SV13) or having the same area. Bins containing the same number of clusters remove the size-of-sample effect. However, we show in Section 3 that our results are not affected by the binning technique.

In general, we find that, within a factor of 2, the SFRs derived using Hα as tracer or stellar count techniques are in very good agreement. Therefore, we conclude that the M83 SFR has been nearly constant in at least the last several tens of Myr as suggested in B12, SV13 and SV14.

We derive lower limits to the CFE, Γ, as a function of galactocentric distance and using the position of the seven pointings across the galactic body. The CFE of the whole cluster population of M83 has a lower limit of ~ 18 per cent. With a wider coverage of the

galaxy and thus a more numerous cluster population, we are able to put strong constraints on the derived Γ values. We see a net decline in Γ from about 26 per cent in the inner bin to 8 per cent in the outer bin. A similar decline is observed in the averaged gas surface density and in the predictions made with the fiducial model by Kruijssen ([2012](#)). We see that the derived values of Γ versus Σ_{SFR} in different regions of M83 follow the Γ–Σ_{SFR} relation of galaxies. We conclude that the relation appears to hold not only on galactic but also on sub-galactic scales. The dependence of Γ on Σ_{SFR} arises from a more fundamental dependence on the gas pressure (or surface density) through the Schmidt–Kennicutt relation. Therefore, the amount of stars locked in clusters appears to be regulated by the same mechanism that regulates the overall star formation process. Similarly to the Schmidt–Kennicutt relation, a well-calibrated Γ–Σ_{SFR} or Γ–$\Sigma(H_2)$ relation can potentially be used to make realistic predictions of cluster formation in cosmological simulations (e.g. Kruijssen [2012](#)). However, more effort is needed for it to empirically link cluster properties to star formation and GMC properties.

Another aspect that can potentially reveal imprints of the galactic environment on the cluster population is the value of the possible truncation in the upper mass end of the ICMF. To investigate this issue, we have built the ICMFs of the cluster population contained in each galactocentric radius bin. We observe a significant steepening of the ICMF as a function of galactocentric distances. Monte Carlo simulations of a single power-law function without upper mass limit are not able to reproduce the observed ICMFs. The steepening can only be consistently reproduced if a Schechter function of slope -2 and exponential cutoff at the high-mass end with a varying M_c is used. M_c decreases significantly in the outer radial bins. This finding is consistent with the observed decrease of the $\Sigma(H_2)$ and likely of the maximum GMC mass. The probability that the ICMF of M83 is drawn by a single power-law mass function of slope -2 is $\sim 4 \times 10^{-3}$. The probability increases significantly if a steeper power-law function ($\alpha \approx -2.2$) is used. The best representation of the M83 ICMF is a Schechter function of slope -2 and $M_c \approx 1.5 \times 10^5$ M$_\odot$. Overall we conclude that the young star cluster mass function can be described by an almost universal ICMF of slope -2 and a variable M_c which appears to be a function of the host galaxy environment. Upcoming systematic surveys of stellar cluster populations will enable us to quantify and constrain this variation further (e.g. Calzetti et al. [2015](#)).

REFERENCES

Adamo A., Bastian N., 2015, in Stahler S. W., ed., to appear in The Birth of Star Clusters. Springer edition, submitted
Adamo A., Östlin G., Zackrisson E., Hayes M., Cumming R. J., Micheva G., 2010, MNRAS, 407, 870
Adamo A., Östlin G., Zackrisson E., 2011, MNRAS, 417, 1904
Adamo A. et al., 2012, MNRAS, 426, 1185
Annibali F., Tosi M., Monelli M., Sirianni M., Montegriffo P., Aloisi A., Greggio L., 2009, AJ, 138, 169
Annibali F., Tosi M., Aloisi A., van der Marel R. P., 2011, AJ, 142, 129
Bastian N., 2008, MNRAS, 390, 759
Bastian N. et al., 2011, MNRAS, 417, L6
Bastian N. et al., 2012, MNRAS, 419, 2606 (B12)
Bertin E., Arnouts S., 1996, A&AS, 117, 393
Bik A., Lamers H. J. G. L. M., Bastian N., Panagia N., Romaniello M., 2003, A&A, 397, 473
Blair W. P. et al., 2014, ApJ, 788, 55
Bolatto A. D., Wolfire M., Leroy A. K., 2013, ARA&A, 51, 207
Calzetti D. et al., 2015, AJ, 149, 51
Cardelli J. A., Clayton G. C., Mathis J. S., 1989, ApJ, 345, 245
Chandar R. et al., 2010, ApJ, 719, 966
Chandar R., Whitmore B. C., Calzetti D., Di Nino D., Kennicutt R. C., Regan M., Schinnerer E., 2011, ApJ, 727, 88
Chandar R., Whitmore B. C., Calzetti D., O'Connell R., 2014, ApJ, 787, 17
Colombo D. et al., 2014, ApJ, 784, 3
Cook D. O. et al., 2012, ApJ, 751, 100
Dale D. A. et al., 2009, ApJ, 703, 517
de Grijs R., Anders P., Bastian N., Lynds R., Lamers H. J. G. L. M., O'Neil E. J., 2003, MNRAS, 343, 1285
Elmegreen B. G., 2002, ApJ, 577, 206
Evans N. J., II et al., 2009, ApJS, 181, 321
Fouesneau M., Lançon A., 2010, A&A, 521, A22
Gieles M., Portegies Zwart S. F., 2011, MNRAS, 410, L6
Gieles M., Larsen S. S., Bastian N., Stein I. T., 2006a, A&A, 450, 129
Gieles M., Larsen S. S., Scheepmaker R. A., Bastian N., Haas M. R., Lamers H. J. G. L. M., 2006b, A&A, 446, L9
Goddard Q. E., Bastian N., Kennicutt R. C., 2010, MNRAS, 405, 857
Hollyhead K., Bastian N., Adamo A., Silva-Villa E., Dale J., Ryon J. E., Gazak Z., 2015, MNRAS, 449, 1106
Holtzman J. A. et al., 1992, AJ, 103, 691
Hunter D. A., Elmegreen B. G., Dupuy T. J., Mortonson M., 2003, AJ, 126, 1836
Johnson K. E., Leitherer C., Vacca W. D., Conti P. S., 2000, AJ, 120, 1273
Jordán A. et al., 2007, ApJS, 171, 101
Kennicutt R. C., Jr, 1998, ApJ, 498, 541
Kennicutt R. C., Evans N. J., 2012, ARA&A, 50, 531
Kennicutt R. C., Jr, Lee J. C., Funes S. J., José G., Sakai S., Akiyama S., 2008, ApJS, 178, 247
Knapen J. H., Sharp R. G., Ryder S. D., Falcón-Barroso J., Fathi K., Gutiérrez L., 2010, MNRAS, 408, 797
Konstantopoulos I. S. et al., 2013, AJ, 145, 137
Kruijssen J. M. D., 2012, MNRAS, 426, 3008
Kruijssen J. M. D., 2014, Class. Quantum Grav., 31, 244006
Kruijssen J. M. D., 2015, MNRAS, submitted
Kruijssen J. M. D., Pelupessy F. I., Lamers H. J. G. L. M., Portegies Zwart S. F., Icke V., 2011, MNRAS, 414, 1339
Kruijssen J. M. D., Maschberger T., Moeckel N., Clarke C. J., Bastian N., Bonnell I. A., 2012, MNRAS, 419, 841
Krumholz M. R., Fumagalli M., da Silva R. L., Rendahl T., Parra J., 2015, preprint ([arXiv:1502.05408](#))
Larsen S. S., 2002, AJ, 124, 1393
Larsen S. S., 2006, preprint ([astro-ph/0606625](#))
Larsen S. S., 2009, A&A, 494, 539
Lim S., Lee M. G., 2015, ApJ, 804, 123
Longmore S. N. et al., 2014, in Beuther H., Klessen R. S., Dullemond C. P., Henning T., eds, Protostars and Planets VI. Univ. Arizona Press, Tucson, p. 291

Lundgren A. A., Wiklind T., Olofsson H., Rydbeck G., 2004a, A&A, 413, 505

Lundgren A. A., Olofsson H., Wiklind T., Rydbeck G., 2004b, A&A, 422, 865

Maíz Apellániz J., Úbeda L., 2005, ApJ, 629, 873

Pasquali A. et al., 2011, AJ, 141, 132

Popescu B., Hanson M. M., 2010, ApJ, 724, 296

Rafelski M., Zaritsky D., 2005, AJ, 129, 2701

Ryon J. E. et al., 2014, AJ, 148, 33

Ryon J. E. et al., 2015, MNRAS, 148, 33

Schechter P., 1976, ApJ, 203, 297

Schlafly E. F., Finkbeiner D. P., 2011, ApJ, 737, 103

Schmidt M., 1959, ApJ, 129, 243

Silva-Villa E., Larsen S. S., 2011, A&A, 529, A25

Silva-Villa E., Larsen S. S., 2012, A&A, 537, A145

Silva-Villa E., Adamo A., Bastian N., 2013, MNRAS, 436, L69 (SV13)

Silva-Villa E., Adamo A., Bastian N., Fouesneau M., Zackrisson E., 2014, MNRAS, 440, L116 (SV14)

Toomre A., 1964, ApJ, 139, 1217

Weidner C., Kroupa P., Larsen S. S., 2004, MNRAS, 350, 1503

Whitmore B. C., 2000, preprint (astro-ph/0012546)

Whitmore B. C., Schweizer F., Leitherer C., Borne K., Robert C., 1993, AJ, 106, 1354

Whitmore B. C., Zhang Q., Leitherer C., Fall S. M., Schweizer F., Miller B. W., 1999, AJ, 118, 1551

Whitmore B. C., Chandar R., Fall S. M., 2007, AJ, 133, 1067

Whitmore B. C. et al., 2011, ApJ, 729, 78

Whitmore B. C., Chandar R., Bowers A. S., Larsen S., Lindsay K., Ansari A., Evans J., 2014, AJ, 147, 78

Wofford A., Leitherer C., Chandar R., 2011, ApJ, 727, 100

Zackrisson E., Rydberg C.-E., Schaerer D., Östlin G., Tuli M., 2011, ApJ, 740, 13

APPENDIX A: THE ICMF OF CLASS 1 AND 2 CLUSTERS IN M83

We report in Fig. A1 the ICMF analysis of class 1 and 2 objects contained in bins of equal area.
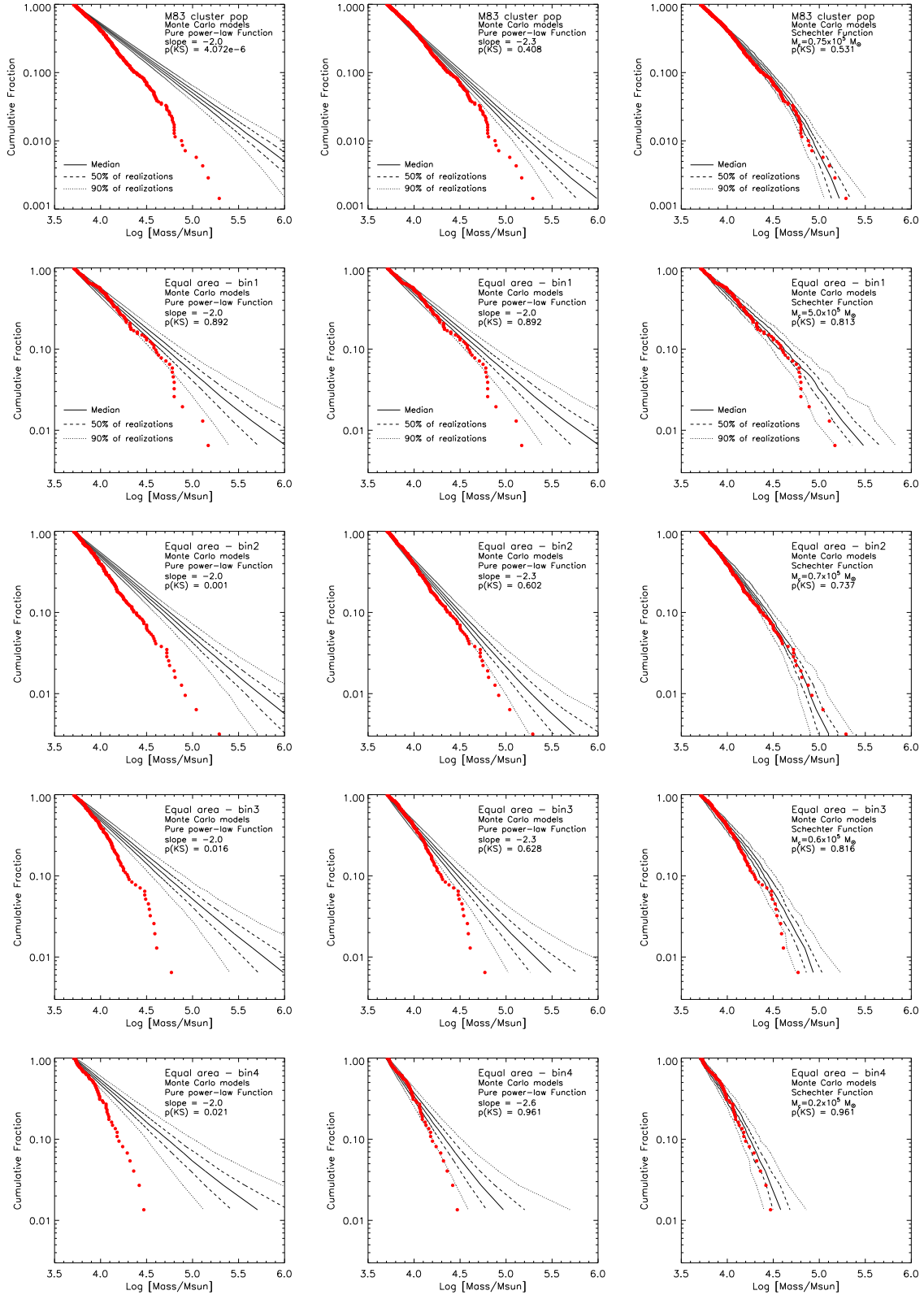
Figure A1. Cumulative ICMFs (red filled dots) of the whole population and of the clusters within bins of same area (from top to bottom). Both class 1 and class 2 systems more massive than 5000 M$_\odot$ and ages between 3 and 100 Myr have been included. Median (solid line), quartiles (dashed line) and extended boundaries (dotted line) of Monte Carlo simulations of cluster populations with the same number of objects as the observed ones are included in each panel. In the first column, to generate the fake populations we assume a pure power-law ICMF with slope −2. In the middle column, we still assume a power-law ICMF but with varying slopes (see insets), chosen to maximize the KS probability that the observed and simulated distributions are drawn from the same parent distribution, p(KS). In the right column, we assume that the ICMF is better described by a Schechter function of slope −2 and an exponential cutoff, M_c, chosen to maximize the KS probability, as indicated in the inset.

APPENDIX B: A COMPLETE COMPILATION OF THE DATA SAMPLES AVAILABLE IN THE LITERATURE

Complete compilation of the data available in the literature and plotted in Figs 4 and 6 is presented in Table B1. The footnote associated with the name of the galaxy gives the reference for all the values reported in the corresponding row, unless a different note on the values specify a different source. Some galaxies are reported more than once, with different values of SFR and Σ_{SFR}, because Γ and related quantities (SFR and Σ_{SFR}) have been derived using only partial coverages of galaxies.

Table B1. (a) Adamo et al. (2011) (blue star symbols in Fig. 6). (b) Larsen (2002) (black triangles in Fig. 6), only a fraction of the original catalogue is listed while the values of the omitted ones are listed with the most recent estimated values available in the literature. (c) The values used for each binning (purple filled dots in Fig. 6) are reported in Table 2 of the main text. (d) Bastian (2008) (black squares in Fig. 6). (e) Whitmore et al. (2014) (orange diamonds in Fig. 6), some of the galaxies in the original list have been omitted because Larsen (2002) presented data with a larger coverage of the galaxy than in this paper. The dwarf galaxies (green star symbols in Fig. 6) include data points from the following papers: (f) Annibali et al. (2011); (g) Pasquali et al. (2011); (h) Goddard et al. (2010); (i) Annibali et al. (2009); (j) Rafelski & Zaritsky (2005); (k) Johnson et al. (2000); (l) Cook et al. (2012); (m) Lim & Lee (2015). (n) In Fig. 4, we show the combined Γ derived by Cook et al. (2012) using all the clusters younger than 10 Myr detected in their dwarf sample. The SFR density reported is not a single value but a range enclosing all the single galactic values. (o) Silva-Villa & Larsen (2011). (p) Ryon et al. (2014). (r) This work. Values obtained considering the age range 1–10 Myr, see Table 2 in the main text for more details.

Galaxy	M_V^{bright} (mag)	SFR ($M_\odot$ yr^{-1})	Σ_{SFR} ($M_\odot$ yr^{-1} kpc^{-2})	Γ (per cent)
ESO 338[a]	−15.50	3.20	1.55	50.0±10.0
Haro 11[a]	−16.16	22.00	2.16	$50.0^{+13.0}_{-15.0}$
ESO 185-IG13[a]	−14.36	6.40	0.52	26.0±5.0
MRK 930[a]	−15.00	5.34	0.59	25.0±10.0
SBS 0335-052E[a]	−14.28	1.30	0.95	49.0±15.0
NGC 247[b]	−10.20	0.0360	0.18×10^{-3}	–
NGC 300[b]	−9.90	0.0779	0.49×10^{-3}	–
NGC 1156[b]	−11.10	0.1842	3.07×10^{-3}	–
NGC 2403[b]	−9.90	0.3376	0.97×10^{-3}	–
NGC 2835[b]	−10.90	0.0920	0.73×10^{-3}	–
NGC 2997[b]	−12.90	1.8604	3.07×10^{-3}	–
NGC 2997[q]	–	–	9.4×10^{-3}	10.0 ± 2.6
NGC 3184[b]	−10.60	0.3956	1.72×10^{-3}	–
NGC 3621[b]	−11.90	0.8801	1.67×10^{-3}	–
NGC 5204[b]	−9.60	0.0315	0.83×10^{-3}	–
M83[b, c]	−11.70	2.2842	13.76×10^{-3}	–
M83 (centre)[h]	–	0.39	0.54	$26.7^{+5.3}_{-4.0}$
M83 (0.45–4.5 kpc)[r]	−11.60	0.82	0.013	18.2±3.0
M83 (outer)[p]	–	0.39	0.013	5.6±0.6
NGC 5585[b]	−10.80	0.0336	0.32×10^{-3}	–
NGC 6744[b]	−11.00	0.4309	0.62×10^{-3}	–
NGC 6946[b]	−13.00	2.5392	4.60×10^{-3}	–
NGC 6946[h] (WFPC2)	–	0.17	4.60×10^{-3}	$12.5^{+1.8}_{-2.5}$
NGC 7424[b]	−11.40	0.1728	0.18×10^{-3}	–
NGC 1741[b]	−15.00	4.8819	12.78×10^{-3}	–
NGC 5253[b]	−11.10	0.2114	7.29×10^{-3}	–
IC 1613[b]	−5.80	0.0004	0.05×10^{-3}	–
LMC	−11.1[h]	0.1201[b]	$1.52\times 10^{-3 b}$	5.8±0.5[h]
NGC 4214[b]	−12.04	0.0798	3.80×10^{-3}	–
DDO 50[b]	−7.91	0.0108	1.26×10^{-3}	–
DDO 168[b]	−7.58	0.0043	0.85×10^{-3}	–
DDO 165[b]	−8.34	0.0005	0.18×10^{-3}	–
Sextans A[b]	−7.12	0.0037	2.29×10^{-3}	–
NGC 3521[b]	−11.50	1.3676	3.58×10^{-3}	–
NGC 4258[b]	−12.60	0.9926	0.70×10^{-3}	–
NGC 5055[b]	−11.40	1.5019	2.98×10^{-3}	–
M51[b]	−12.80	4.7454	8.21×10^{-3}	–
NGC 7252[d]	−13.40	5.40	–	–
NGC 6240[d]	−16.40	140.00	–	–
NGC 2207[d]	−13.60	2.20	–	–
NGC 1275[d]	−15.30	12.40	–	–

Table B1 – continued

Galaxy	M_V^{bright} (mag)	SFR ($M_\odot$ yr^{-1})	Σ_{SFR} ($M_\odot$ yr^{-1} kpc^{-2})	Γ (per cent)
M82[d]	-14.80	7.00	–	–
NGC 3597[d]	-13.30	10.80	–	–
IRAS 19115[d]	-16.80	192.00	–	–
NGC 1533[d] (A1)	-7.17	0.37×10^{-3}	–	–
NGC 1533[d] (A2)	-5.71	0.25×10^{-3}	–	–
NGC 1533[d] (A3)	-6.16	0.18×10^{-3}	–	–
NGC 2623[d]	-14.50	51.00	–	–
NGC 3256[d]	-15.70	46.00	0.62	$22.9^{+7.3h}_{-9.8}$
NGC 7673[d]	-14.70	4.90	–	–
NGC 6745[d]	-15.00	12.20	–	–
NGC 1140[d]	-14.80	0.80	–	–
Milky Way[h]	–	0.1508	0.012	$7.0^{+7.0}_{-3.0}$
NGC 45[e]	-10.83	0.12	–	–
NGC 45[p]	–	0.05	1.02×10^{-3}	5.2 ± 0.3
NGC 406[e]	-11.75	0.29	–	–
NGC 628[e]	-11.84	0.23	–	–
NGC 1300[e] (F1)	-11.00	0.30	–	–
NGC 1300[e] (F2)	-11.52	0.32	–	–
NGC 1309[e]	-13.80	1.70	–	–
NGC 1313[e]	-10.98	0.22	–	–
NGC 1313[p]	–	0.68	0.011	3.2 ± 0.2
NGC 1483[e]	-10.01	0.11	–	–
NGC 3627[e]	-11.97	0.37	–	–
NGC 4038[e]	-15.25	2.43	–	–
NGC 4394[e]	-10.25	0.14	–	–
NGC 4395[e]	-9.79	0.07	–	–
NGC 4395[p]	–	0.17	4.66×10^{-3}	1.0 ± 0.6
NGC 4736[e]	-10.44	0.04	–	–
NGC 5055[e]	-9.61	0.02	–	–
M101[e] (F1)	-11.38	0.25	–	–
M101[e] (F2)	-11.57	0.20	–	–
NGC 6503[e]	-10.51	0.07	–	–
NGC 7793[e]	-9.65	0.07	–	–
NGC 7793[p]	–	0.15	6.51×10^{-3}	2.5 ± 0.3
NGC 4449[f]	-12.60	1.0	0.04	9.0
NGC 1569[g]	-13.9[b]	0.36[g]	0.03[g]	13.9 ± 0.8[h]
NGC 1705[i]	-13.8	0.31	0.046	–
SMC[j]	-9.94	0.043	0.001	$4.2^{+0.2h}_{-0.3}$
He2-10[k]	-12.5	0.20	0.20	–
NGC 2366[l]	-8.52	0.094	2.4×10^{-3}	–
UGC 4305[l]	-8.88	0.114	2.2×10^{-3}	–
UGC 4459[l]	-7.9	0.003	1.0×10^{-3}	–
UGC 5336[l]	-8.59	0.004	0.000 37	–
IC 2574[l]	-9.12	0.11	1.2×10^{-3}	–
UGC 5692[l]	-9.44	7.34×10^{-3}	0.5×10^{-3}	–
UGCa 292[l]	-7.46	5.15×10^{-3}	0.01	–
UGC 8201[l]	-9.16	31.6×10^{-3}	2.1×10^{-3}	–
UGC 9128[l]	-5.45	0.3×10^{-3}	0.3×10^{-3}	–
UGC 9240[l]	-5.90	5.24×10^{-3}	1.0×10^{-3}	–
Dwarf sample[o]	–	–	$[0.01, 10.0]\times10^{-3}$	5.0
IC 10[m]	-10.4	0.07	0.03	4.2

This paper has been typeset from a T$_{\mathrm{E}}$X/L$^{\mathrm{A}}$T$_{\mathrm{E}}$X file prepared by the author.